J. Fluid Mech. (2000), *vol.* 405, *pp.* 325–349. Printed in the United Kingdom

© 2000 Cambridge University Press

Simulation of swept-wing vortices using nonlinear parabolized stability equations

By TIM S. HAYNES[1] AND HELEN L. REED[2]

[1]Hughes Space and Communications Company, El Segundo, CA 90245-0902, USA

[2]Department of Aerospace and Mechanical Engineering, Arizona State University, Tempe, AZ 85287-6106, USA

(Received 22 September 1997 and in revised form 28 September 1999)

The nonlinear development of stationary crossflow vortices over a 45° swept NLF(2)-0415 airfoil is studied. Previous investigations indicate that the linear stability theory (LST) is unable to accurately describe the unstable flow over crossflow-dominated configurations. In recent years the development of nonlinear parabolized stability equations (NPSE) has opened new pathways toward understanding unstable boundary-layer flows. This is because the elegant inclusion of nonlinear and non-parallel effects in the NPSE allows accurate stability analyses to be performed without the difficulties and overhead associated with direct numerical simulations (DNS). NPSE results are presented here and compared with experimental results obtained at the Arizona State University Unsteady Wind Tunnel. The comparison shows that the saturation of crossflow disturbances is responsible for the discrepancy between LST and experimental results for cases with strong favourable pressure gradient. However, for cases with a weak favourable pressure gradient the stationary crossflow disturbances are damped and nonlinearity is unimportant. The results presented here clearly show that for the latter case curvature and non-parallel effects are responsible for the previously observed discrepancies between LST and experiment. The comparison of NPSE and experimental results shows excellent agreement for both configurations.

Through this work, a detailed quantitative comparison and validation of NPSE with a careful experiment has now been provided for three-dimensional boundary layers. Moreover, the results validate the experiments of Reibert *et al.* (1996), and Radeztsky *et al.* (1993, 1994) suggesting that their databases can be used by future researchers to verify theories and numerical schemes. The results show the inadequacy of linear theories for modelling these flows for significant crossflow amplitude and demonstrate the effects of weak curvature to be more significant than slight changes in basic state, especially near neutral-stability locations.

1. Introduction

The wings of high-speed aircraft are swept resulting in three-dimensional boundary layers over the wing surface. A typical three-dimensional boundary-layer velocity profile is shown in figure 1. For the boundary layer over an infinite-span swept airfoil there are no gradients in the spanwise (z) direction and the pressure is nearly constant across the boundary layer itself so that pressure varies only in the direction normal to the leading edge along the body. This causes the inviscid streamlines to be curved and deflected inboard near the leading edge. The local-inviscid direction is defined as the direction tangent to the velocity at the edge of the boundary layer.

https://doi.org/10.1017/S0022112099007260 Published online by Cambridge University Press

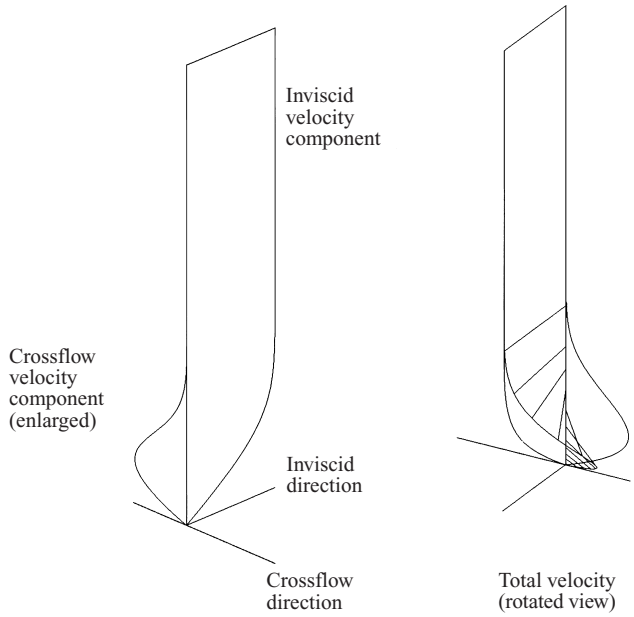


FIGURE 1. Typical three-dimensional boundary-layer profile.

The crossflow direction is then defined to be perpendicular to both the wall-normal and local-inviscid directions such that the coordinate system is right-handed. Since the pressure gradient is in a direction normal to the leading edge ($x = 0$), there will be pressure gradients associated with both the inviscid and crossflow directions. At a point located just outside the boundary layer, the viscous forces are negligible so the inertia forces are in balance with the pressure forces. Moving toward the wall, the viscous forces undo this balance. The crossflow velocity component is generated to compensate for this imbalance.

The crossflow velocity must be zero at the wall ($y = 0$) and approach zero asymptotically as $y \to \infty$. Thus, there must be an inflection point somewhere in the velocity profile. This inflection point is the harbinger of a dynamic instability.

When the crossflow velocity component is present, disturbances entering the boundary layer interact with roughness near the leading edge to form travelling (unsteady) crossflow vortices. In low-turbulence-level environments roughness may introduce stationary crossflow vortices. Linear stability theory predicts that the most amplified crossflow disturbances are travelling waves; however experiments have since shown that either travelling or stationary disturbances will dominate the transition process depending on the turbulence level outside the boundary layer. For detailed discussions refer to the literature (Bippes 1991; Bippes, Müller & Wagner 1991; Bippes & Müller 1990; Müller & Bippes 1989; Deyhle, Höhler & Bippes 1993). They showed that the travelling crossflow disturbance will dominate when the free-stream environment has a high level of unsteady disturbances, while the stationary crossflow disturbance is observed for low-turbulence environments. The low-turbulence-level environment is generally regarded as a more accurate depiction of flight conditions. They also noticed saturation of the stationary crossflow waves during the low-turbulence-level experiments. The conclusion of Bippes (1991) is that linear stability theory (LST) fails to predict the growth rates for three-dimensional flows. Discrepancies with LST are also observed in the experimental investigations of Kachanov & Tararykin (1990),

https://doi.org/10.1017/S0022112099007260 Published online by Cambridge University Press

Radeztsky, Reibert & Saric (1994), and Reibert *et al.* (1996). Some of these results are recapitulated in Arnal (1994) and Reed, Saric & Arnal (1996). It is clear from these experiments that LST is unable to cope with crossflow-dominated unstable flows.

Recently the parabolized stability equations (PSE) have been developed which exploit the convective nature of the disturbance to convert the disturbance equations into a system of parabolic differential equations. This allows the spatial evolution of disturbances to be studied using an efficient marching algorithm. Several investigators have successfully applied this technique to various geometries including flat plates, swept Hiemenz flow, cones, and infinite swept wings (Herbert 1994, 1997; Arnal *et al.* 1997; Malik 1997; Bertolotti 1990, 1996).

In particular, using nonlinear parabolized stability equations (NPSE), Bertolotti (1996) studied the evolution of disturbances for the above-referenced experiments of Bippes and colleagues on a swept flat plate. He cleverly modelled the receptivity of three-dimensional boundary layers to an array of surface bumps accounting for both the streamwise and spanwise variations of the basic state and then carried the PSE calculations on through to the amplitude-saturated states in the strongly nonlinear regime. His results agree quantitatively with the experiments.

The NPSE appear to be the new state-of-the-art prediction and analysis tool for boundary-layer stability investigations. The success of other investigators motivates this attempt to apply NPSE for the swept-wing case of Reibert *et al.* (1996) with the objective of examining the effects of nonlinearity, curvature, pressure gradient, chord Reynolds number (R_C), and non-parallelism on crossflow disturbances.

2. Numerical formulation

2.1. *Basic state*

The present work investigates the stability of incompressible laminar boundary-layer flows over swept wings. The configuration chosen for this investigation is the NLF(2)-0415 airfoil at -4° angle-of-attack (AOA). The computational results complement the experimental efforts of Reibert *et al.* (1996) who use the same configuration at the Arizona State University Unsteady Wind Tunnel. This is an ideal setting for the growth of crossflow disturbances and should suppress the growth of any Tollmien–Schlichting (TS) waves that may be present. The basic-state flow is assumed to be invariant in the spanwise (z) direction. The pressure distribution over the airfoil is determined by the MCARF code (Stevens, Goradia & Braden 1971). This inviscid solution provides the necessary edge boundary conditions for the boundary-layer equations.

The compressible boundary-layer equations are formulated in body-intrinsic coordinates. Although the configuration of interest for this paper is an incompressible swept-wing flow, a compressible approach is developed so the authors may conduct further analysis for high-speed flows. The following transformation is used to remove the singularity at the attachment line and reduce the boundary-layer growth in the computational domain:

$$\xi(\bar{x}) = \bar{x}, \tag{2.1}$$

$$\zeta(\bar{x}, y) = \frac{1}{\sqrt{2\xi}} \int_0^y \rho(\bar{x}, \bar{y})\, \mathrm{d}\bar{y}, \tag{2.2}$$

where $\bar{x}$ and y are the dimensionless streamwise and normal coordinates respectively:

$$\bar{x} = \frac{x^*}{R_o \delta_o}, \qquad y = \frac{y^*}{\delta_o}. \tag{2.3}$$

https://doi.org/10.1017/S0022112099007260 Published online by Cambridge University Press

Here δ_o is the boundary layer reference length and R_o is the corresponding Reynolds number, $R_o = U_r\delta_o/\nu_r$, where U_r and ν_r are the free-stream speed and kinematic viscosity, respectively.

The transformed boundary-layer equations reduce to ordinary differential equations at the attachment line ($\xi = 0$) which are solved to provide initial conditions for the streamwise marching. The Chebyshev collocation method with Richardson iteration and second-order finite-difference preconditioning is used to discretize these equations. Fifth-order backward finite differencing is used for the streamwise derivatives. This approach is similar to that used by Pruett & Streett (1991).

The solution for flow over a flat plate at zero AOA is computed to validate the code and determine the appropriate grid parameters. Numerical experiments show that the grid is well resolved when 81 collocation points are used. No clustering is used other than the natural clustering occurring as a result of the transformation to Chebyshev space. The optimum relaxation parameter (τ) and domain truncation location (ζ_{trunc}) are also determined by numerical experiment to be 0.2 and 12.0, respectively. The convergence tolerance imposed on the residuals at the collocation points is $\epsilon_{tol} = 10^{-8}$.

2.2. *Disturbances*

The total dimensionless flow quantities are separated into steady basic-state and unsteady disturbance quantities:

$$\phi(x,y,z,t) = \Phi(x,y) + \phi'(x,y,z,t), \tag{2.4}$$

where $\phi = (\rho, u, v, w, T)$. The disturbance equations are obtained by substituting this form into the Navier–Stokes equations and subtracting terms which consist of purely basic-state quantities. The curvature terms are retained in the equations unless noted otherwise. The dimensionless compressible disturbance equations in body-intrinsic orthogonal curvilinear coordinates in matrix form are

$$\mathscr{B}_0\frac{\partial \boldsymbol{\phi}'}{\partial t} + \mathscr{B}_1\frac{\partial \boldsymbol{\phi}'}{\partial x} + \mathscr{B}_2\frac{\partial \boldsymbol{\phi}'}{\partial y} + \mathscr{B}_3\frac{\partial \boldsymbol{\phi}'}{\partial z} + \mathscr{C}_1\frac{\partial^2 \boldsymbol{\phi}'}{\partial x^2} + \mathscr{C}_2\frac{\partial^2 \boldsymbol{\phi}'}{\partial y^2} + \mathscr{C}_3\frac{\partial^2 \boldsymbol{\phi}'}{\partial z^2}$$
$$+\mathscr{D}_1\frac{\partial^2 \boldsymbol{\phi}'}{\partial x\partial y} + \mathscr{D}_2\frac{\partial^2 \boldsymbol{\phi}'}{\partial x\partial z} + \mathscr{D}_3\frac{\partial^2 \boldsymbol{\phi}'}{\partial y\partial z} + \mathscr{D}_4\boldsymbol{\phi}' = \mathscr{N}. \tag{2.5}$$

For brevity, the components of the coefficient matrices are not presented. The non-zero elements of the coefficient matrices can be found in Haynes (1996) and are also available from the Journal of Fluid Mechanics Editorial Office on request.

For the linear PSE (LPSE) the nonlinear products of ϕ' are dropped and the disturbance is decomposed into a rapidly varying 'wave function' and a slowly varying 'shape function'. This is accomplished using a multiple-scales approach recalling that $R_o = U_r\delta_o/\nu$:

$$\boldsymbol{\phi}'(x,y,z,t) = \underbrace{\tilde{\boldsymbol{\phi}}(\bar{x},y)}_{\text{shape function}}\ \underbrace{\chi(x,z,t)}_{\text{wave function}} + \text{c.c.}, \tag{2.6}$$

where

$$\frac{\partial\chi}{\partial x} = \mathrm{i}\alpha(\bar{x}), \quad \frac{\partial\chi}{\partial z} = \mathrm{i}\beta, \quad \frac{\partial\chi}{\partial t} = -\mathrm{i}\omega. \tag{2.7}$$

Here β and ω are the dimensionless spanwise wavenumber and frequency of the disturbance. The 'shape function' $\tilde{\phi}$ and streamwise wavenumber α depend on the slowly varying scale $\bar{x}$ while the 'wave function' χ depends on the rapidly varying

https://doi.org/10.1017/S0022112099007260 Published online by Cambridge University Press

scale x ($x = R_o\bar{x}$). This gives the following form for the streamwise derivatives of disturbance quantities:

$$\left.\begin{aligned}\frac{\partial \boldsymbol{\phi}'}{\partial x} &= \left\{\frac{1}{R_o}\frac{\partial \tilde{\boldsymbol{\phi}}}{\partial \bar{x}} + \mathrm{i}\alpha\tilde{\boldsymbol{\phi}}\right\}\chi + \text{c.c.},\\ \frac{\partial^2 \boldsymbol{\phi}'}{\partial x^2} &= \left\{\frac{1}{R_o^2}\frac{\partial^2 \tilde{\boldsymbol{\phi}}}{\partial \bar{x}^2} + \frac{2\mathrm{i}\alpha}{R_o}\frac{\partial \tilde{\boldsymbol{\phi}}}{\partial \bar{x}} + \frac{\mathrm{i}\tilde{\boldsymbol{\phi}}}{R_o}\frac{\mathrm{d}\alpha}{\mathrm{d}\bar{x}} - \alpha^2\tilde{\boldsymbol{\phi}}\right\}\chi + \text{c.c.}\end{aligned}\right\} \tag{2.8}$$

The approach taken here is to simply substitute these forms into the disturbance equations and neglect the $O(1/R_o^2)$ second-derivative term. This yields the system of equations:

$$\left(\mathscr{L}_0 + \mathscr{L}_1\right)\tilde{\boldsymbol{\phi}} + \mathscr{L}_2\frac{\partial \tilde{\boldsymbol{\phi}}}{\partial \bar{x}} + \tilde{\boldsymbol{\phi}}\mathscr{L}_3\frac{\mathrm{d}\alpha}{\mathrm{d}\bar{x}} = 0. \tag{2.9}$$

Here $\mathscr{L}_0$ contains the linear parallel terms, $\mathscr{L}_1$ contains the non-parallel basic-state terms, $\mathscr{L}_2$ and $\mathscr{L}_3$ arise due to the non-parallel disturbance terms. The $\mathscr{L}_0$ operator reduces to the Orr–Sommerfeld operator for incompressible flows.

This system of equations is parabolic and thus requires boundary and initial conditions. The disturbance velocity and temperature are set equal to zero at the wall and as $y \to \infty$

$$\tilde{u} = \tilde{v} = \tilde{w} = \tilde{T} = 0. \tag{2.10}$$

This corresponds to no-slip and no-temperature-fluctuation boundary conditions at the wall, and vanishing temperature and velocity disturbances as $y \to \infty$. These boundary conditions are reasonable for the flow of gas over a solid wall (Mack 1969). Since there is no physical boundary condition for $\tilde{\rho}$ at the wall and as $y \to \infty$, the mass equation is applied to close the system. Initial conditions are obtained by solving the linear (parallel) stability equations.

There still remains the matter of the ambiguity in x-dependence between $\tilde{\phi}$ and χ in the decomposition (2.6). This is resolved by imposing a normalization condition on the shape function:

$$\varrho = \int_0^\infty \tilde{u}^\dagger\frac{\partial \tilde{u}}{\partial \bar{x}}\mathrm{d}y = 0, \tag{2.11}$$

where $\dagger$ denotes the complex conjugate. This normalization ensures that any rapid changes in the streamwise direction will be 'absorbed' by the 'wave function' so that the 'shape function' will vary slowly in this direction. This allows the $O(1/R_o^2)$ diffusion term to be discarded. An integral normalization is chosen here rather than one applied at the location of the shape-function maximum because the shape functions may develop multiple maxima during nonlinear streamwise marching.

The NPSE are derived in a fashion similar to the LPSE. Each disturbance quantity is transformed spectrally in the spanwise and temporal directions using

$$\boldsymbol{\phi}'(x,y,z,t) = \sum_{n=-\infty}^{\infty}\sum_{k=-\infty}^{\infty}\underbrace{\tilde{\boldsymbol{\phi}}_{(n,k)}(\bar{x},y)}_{\text{shape function}}\underbrace{\mathscr{A}_{(n,k)}(x)\,\mathrm{e}^{\mathrm{i}(k\beta_o z - n\omega_o t)}}_{\text{wave function}} \tag{2.12}$$

where

$$\frac{\mathrm{d}\mathscr{A}_{(n,k)}}{\mathrm{d}x} = \mathscr{A}_{(n,k)}\mathrm{i}\alpha_{(n,k)}(\bar{x}). \tag{2.13}$$

Here each 'mode', (n,k), is considered to be the product of a 'shape function' and a 'wave function'. Substituting this disturbance form into the Navier–Stokes

https://doi.org/10.1017/S0022112099007260 Published online by Cambridge University Press

equations gives

$$\sum_{n=-\infty}^{\infty}\sum_{k=-\infty}^{\infty}\left\{\left(\mathscr{L}_0+\mathscr{L}_1\right)\tilde{\boldsymbol{\phi}}+\mathscr{L}_2\frac{\partial\tilde{\boldsymbol{\phi}}}{\partial\bar{x}}+\frac{\mathrm{d}\alpha}{\mathrm{d}\bar{x}}\mathscr{L}_3\tilde{\boldsymbol{\phi}}\right\}_{(n,k)}\mathscr{A}_{(n,k)}\,\mathrm{e}^{\mathrm{i}(k\beta_o z-n\omega_o t)}=\mathscr{N}. \tag{2.14}$$

The portion in brackets on the left-hand side contains the same quantities as in equation (2.9) for the LPSE except the quantities α and $\tilde{\boldsymbol{\phi}}$ now carry the subscripts (n,k) identifying them with a particular mode, and ω and β appearing in equation (2.9) must be replaced with $n\omega_o$ and $k\beta_o$ respectively. Here ω_o and β_o are the fundamental frequency and spanwise wavenumber, respectively, of the disturbance. The marching procedure described for the LPSE is implemented for the NPSE by requiring each mode to individually satisfy equation (2.11). The boundary conditions for individual NPSE modes are the same as those for LPSE (2.10) except for mean flow distortion $(k=0, n=0)$, where the normal velocity condition as $y\to\infty$ is replaced by

$$\frac{\partial\tilde{v}_{(0,0)}}{\partial y}=0. \tag{2.15}$$

An NPSE program was written to solve equation (2.14) using fourth-order-accurate finite differences in the normal direction. The explicit Euler scheme is used for the first streamwise step, beyond which second-order backward finite differences are used. The basic-state quantities appearing in the NPSE are computed using the boundary-layer program discussed in the previous section. The nonlinear terms can be omitted within the program to solve the LPSE (equation (2.9)). The ability to omit or retain curvature terms is also designed into the program.

The program design also facilitates LST solutions by setting $\mathscr{L}_1$, $\mathscr{L}_2$, and $\mathscr{L}_3$ equal to zero and modifying the boundary conditions. In this case the equations constitute a nonlinear eigenvalue problem. A local solution method is used where the streamwise disturbance velocity boundary condition is replaced with

$$\tilde{\rho}=1 \tag{2.16}$$

which simply normalizes the eigenvector. Enforcing this inhomogeneous boundary condition in conjunction with a guess for the eigenvalue (α_g) results in a boundary value problem for $\tilde{\boldsymbol{\phi}}$:

$$\mathscr{L}_0(\alpha_g)\tilde{\boldsymbol{\phi}}=0, \tag{2.17}$$

with

$$\tilde{\rho}=1,\quad \tilde{v}=\tilde{w}=\tilde{T}=0\quad \text{at } y=0, \tag{2.18}$$

and

$$\tilde{u}=\tilde{v}=\tilde{w}=\tilde{T}=0\quad \text{as } y\to\infty. \tag{2.19}$$

This system is solved for $\tilde{\boldsymbol{\phi}}$ and α is updated using Newton's method until the boundary condition $\tilde{u}=0$ is satisfied at the wall. For further details see Malik, Chuang & Hussaini (1982).

This local method requires an initial guess for the eigenvalue (α_g). A global eigensolver was written to provide the initial eigenvalues using a Chebyshev collocation discretization in the y-direction. The nonlinear eigenvalue problem is transformed to a linear problem by extending the eigenvector (Bridges & Morris 1984). Once the eigenvalue is known at an initial streamwise station, the LST program can be marched downstream using the eigenvalues from previous streamwise locations as initial guesses. Solutions from the LST are also used as initial conditions for the LPSE and NPSE marching.

https://doi.org/10.1017/S0022112099007260 Published online by Cambridge University Press

In the NPSE calculations presented here, only the fundamental $(0,1)$ mode is excited initially and harmonics up to mode $(0,8)$ are turned on when the maximum of $\hat{u}_{rms}$, defined later in this section, for a 'neighbouring' mode becomes $O(10^{-8})$. The initial shape functions for the harmonics are obtained by solving their local inhomogeneous mode equations with forcing due to nonlinear interactions. The initial complex wavenumber is determined by averaging the complex wavenumbers of the modes contributing to the nonlinear forcing. Because the Mach number is low, only the quadratic nonlinear terms are computed. A small marching step ($\Delta(x^*/c) \approx 0.001$) is taken in order to obtain high streamwise resolution.

The flat-plate boundary-layer flow is used to test the code and determine the appropriate grid parameters. Grid refinement is achieved by performing linear parallel stability calculations by turning off the nonlinear and non-parallel terms in the NPSE code. The grid is refined until the eigenvalues of the linear stability formulation converge. To further verify the NPSE code, the analysis of Bertolotti (1990) for two-dimensional disturbances in an incompressible flat-plate boundary layer is repeated and excellent agreement is obtained.

We now turn our focus to applying these programs to the investigation of swept-wing crossflow vortices. In the experiment of Reibert (1996), the spanwise wavelength is forced by an array of roughness elements at dimensional position $x^* = 0.023$ chord (c) with 12 mm spanwise spacing. To model this situation with the NPSE, only the fundamental spanwise wavenumber corresponding to a spanwise wavelength of 12 mm is excited initially. This mode is initiated at $x^*/c = 0.05$ using the global eigensolver to acquire the initial conditions. The initial amplitude is chosen such that the disturbance mode shape maximum amplitude, $[u_{rms}]_{max}$ matches that of the experiment at $x^*/c = 0.10$. It typically required three iterations to match the experimental $[u_{rms}]_{max}$ amplitude at $x^*/c = 0.10$ by choosing $[u_{rms}]_{max}$ at $x^*/c = 0.05$. The NPSE is started upstream of the region for experimental comparisons to allow numerical transients to die out. The u_{rms} profiles at an arbitrary streamwise location, $x = \hat{x}$, are defined as

$$u_{rms}(\hat{x}, y) \equiv \left[\frac{1}{z_{max}} \int_0^{z_{max}} \left\{ \frac{u^*(\hat{x}, y, z)}{u_e(\hat{x})} - u_{avg}(\hat{x}, y) \right\}^2 \mathrm{d}z \right]^{1/2}, \tag{2.20}$$

where

$$u_{avg}(\hat{x}, y) \equiv \frac{1}{z_{max}} \int_0^{z_{max}} \frac{u^*(\hat{x}, y, z)}{u_e(\hat{x})} \mathrm{d}z, \tag{2.21}$$

$$[u_{rms}]_{max} \equiv \max_y u_{rms}(\hat{x}, y), \tag{2.22}$$

and z_{max} is the spanwise extent of sampling. In the above definitions u^* is the dimensional velocity measured by the hot-wire probe of the experiment, and u_e is its dimensional value at the boundary-layer edge. With this definition, the u_{rms} profiles contain information contributed from all the spanwise disturbance modes $((0,1),(0,2),\ldots)$ but not the contribution from the mean-flow distortion, mode $(0,0)$. This allows the disturbance to be separated from the basic state so that N-factor calculations can be performed from experimental measurements. The u_{avg} profiles are the sum of the 'undisturbed' basic state and the mean-flow distortion which develops due to nonlinear interactions.

A second quantity will be used to compare the amplitudes of the computed velocity profiles for each of the individual NPSE modes to allow mode–mode

https://doi.org/10.1017/S0022112099007260 Published online by Cambridge University Press

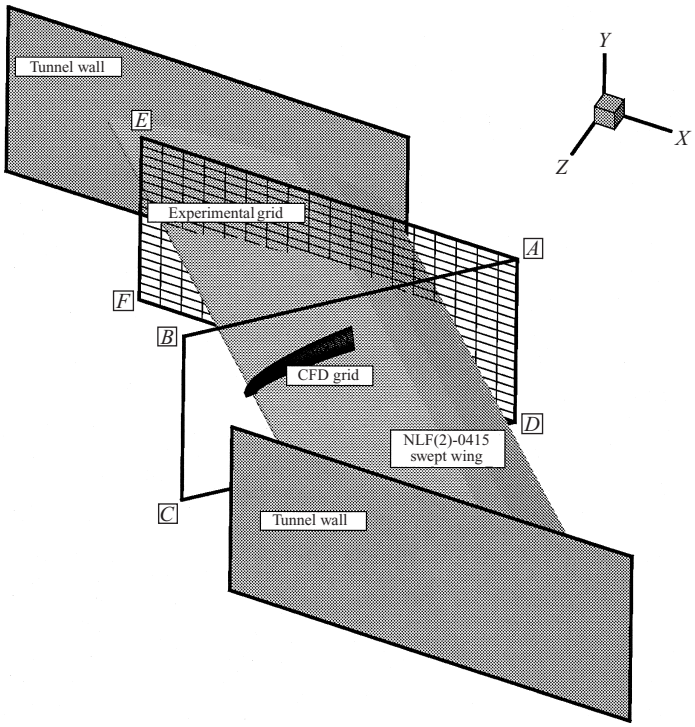


FIGURE 2. NLF(2)-0415 airfoil at −4° angle-of-attack.

amplitude comparisons:

$$\hat{u}_{rms}(\hat{x},y) \equiv \left[\frac{\beta_o}{2\pi}\int_0^{2\pi/\beta_o}\left\{\tilde{u}_{(0,k)}(\hat{x},y,z)\mathscr{A}_{(0,k)}(\hat{x})\mathrm{e}^{\mathrm{i}k\beta_o z}+\mathrm{c.c.}\right\}^2\mathrm{d}z\right]^{(1/2)}$$
$$= \begin{cases} \sqrt{2}|\tilde{u}_{(0,k)}||\mathscr{A}_{(0,k)}| & \text{for } k\neq 0 \\ \frac{1}{2}\sqrt{2}|\tilde{u}_{(0,k)}||\mathscr{A}_{(0,k)}| & \text{for } k=0, \end{cases} \tag{2.23}$$

$$[\hat{u}_{rms}]_{max} \equiv \max_y \hat{u}_{rms}(\hat{x},y). \tag{2.24}$$

It is important to distinguish that the definition of $[\hat{u}_{rms}]_{max}$ is used during the NPSE calculation to determine where neighbouring modes should be activated and for post-calculation comparisons between NPSE modes, while the definition of $[u_{rms}]_{max}$ is used for comparisons with experimental data.

3. Baseline results

Different coordinate systems are used for the computations and experiments. Figure 2 depicts the swept-wing configuration as it is mounted in the unsteady wind tunnel. The wall liners in the tunnel duplicate the inviscid streamlines so that a spanwise-independent basic-state flow is achieved. In this figure the free-stream flow is from left to right and parallel to plane $ADFE$. The plane $ABCD$ slices the airfoil perpendicular to the leading edge so the angle $\angle BAE = \Lambda$, the sweep angle, which is 45° for this case. Plane $ABCD$ represents the plane in which the computations are performed. The computational grid is body-intrinsic so the local x-direction lies in plane $ABCD$

https://doi.org/10.1017/S0022112099007260 Published online by Cambridge University Press

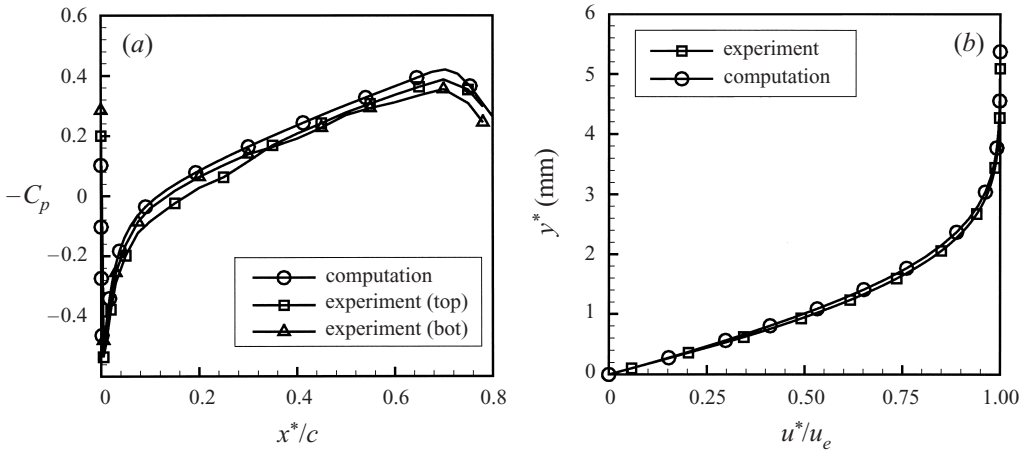


FIGURE 3. Comparison of computational and experimental (*a*) pressure coefficients and (*b*) velocity profiles at $x^*/c = 0.50$ (symbols for reference only).

and is tangent to the airfoil surface, the local y-direction lies in plane $ABCD$ and is normal to the airfoil surface, and the local z-direction is perpendicular to the plane $ABCD$.

For the experiment, a hot-wire probe is mounted at the end of a sting and aligned to traverse in a different coordinate system, (X, Y, Z), which is shown in figure 2. During the set-up procedure the hot wire is aligned parallel to the Z-axis and thus reports the magnitude of the projection of the *total* velocity vector onto plane $ADFE$. The probe is rotated twice: once about the Z-axis to bring it into contact with the airfoil surface, and a second time about its own axis until both prongs of the probe are tangent to the airfoil surface. Boundary-layer profiles are then obtained by traversing in the Y-direction. In all of the following comparisons of computational and experimental results, the computational results are transformed to the experimental coordinate system and the probe velocity is computed taking the rotations mentioned above into consideration.

Before planning the experimental and numerical investigation, the N-factors for several spanwise wavelengths are computed using LST. The free-stream turbulence level is very low ($O(10^{-4})$) so that stationary crossflow vortices are expected to appear and dominate transition. The N-factor corresponding to a stationary crossflow disturbance with spanwise wavelength of 12 mm appears to experience the largest growth for this configuration (NLF(2)-0415 airfoil at -4° AOA) and thus is chosen as the fundamental mode for the experiments and the computations. The crossflow vortices are generated during the experiment by placing 6 μm high roughness elements on the wing near the leading edge ($x^*/c = 0.023$) separated by 12 mm in the spanwise direction (z). It should be noted that the roughness spacing of 12 mm in the spanwise direction along the wing is different from the spacing of the crossflow vortices themselves since they are approximately aligned in the local inviscid direction. See Reibert *et al.* (1996) for details of the experimental facility. Results presented in this section constitute a baseline case from which parameter studies are made.

3.1. *Basic state*

The inviscid flow over the swept wing is computed using the MCARF panel code (Stevens *et al.* 1971). Figure 3(*a*) shows a comparison of experimental and numerical

https://doi.org/10.1017/S0022112099007260 Published online by Cambridge University Press

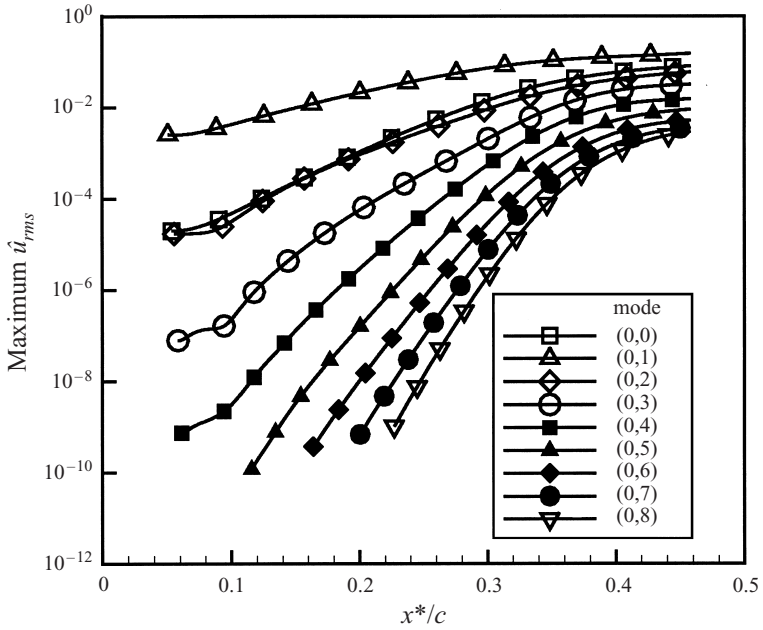


FIGURE 4. Computed $[\hat{u}_{rms}]_{max}$ magnitudes for the various modes $R_C = 2.4 \times 10^6$ (symbols for reference only).

pressure coefficient (C_p) versus percent chord. This pressure distribution provides the edge boundary conditions for the boundary-layer code. Figure 3(*b*) shows the comparison of experimental and numerical streamwise boundary-layer profiles at $x^*/c = 0.50$ for $R_C = 1.6 \times 10^6$. The experimental profile is taken for a smooth leading edge (no artificial roughness elements) so the flow is laminar at this chord position. The overall agreement is good.

3.2. *Disturbances*

In the experiment of Reibert *et al.* (1996), 6 μm high roughness elements are placed near the wing leading edge with 12 mm spanwise spacing. The chord Reynolds number and Mach number for this case are $R_C = 2.4 \times 10^6$ and $M = 0.065$. The entire unstable boundary layer from the initial condition at $x^*/c = 0.05$ to $x^*/c = 0.45$ is computed with the boundary-layer and NPSE codes. As mentioned before, the initial condition is obtained from LST and the initial amplitude is chosen such that the disturbance $[u_{rms}]_{max}$ amplitude matches that of the experiment at $x^*/c = 0.10$.

The experimentally observed transition location for this configuration is $x^*/c \approx 0.52$. Experimental results are available for comparison in this range in 5% chord location increments (i.e. data at $x^*/c = 0.05$, $x^*/c = 0.10$, ... $x^*/c = 0.45$).

Figure 4 shows the $[\hat{u}_{rms}]_{max}$ amplitudes versus chord position for several NPSE modes. Modes (0, 2)–(0, 4) and the mean-flow distortion (0, 0) are activated almost immediately by applying the criterion that modes be activated when the maximum $\hat{u}_{rms}$ amplitude of a neighbouring mode exceeds $O(10^{-8})$. Modes (0, 5)–(0, 8) are activated sequentially as the marching proceeds. Although this scheme would dictate the inclusion of modes (0, 9) and higher (since the maximum $\hat{u}_{rms}$ amplitude of mode (0, 8) exceeds $O(10^{-8})$ at $x^*/c \approx 0.25$), mode (0, 8) is two orders of magnitude smaller

https://doi.org/10.1017/S0022112099007260 Published online by Cambridge University Press

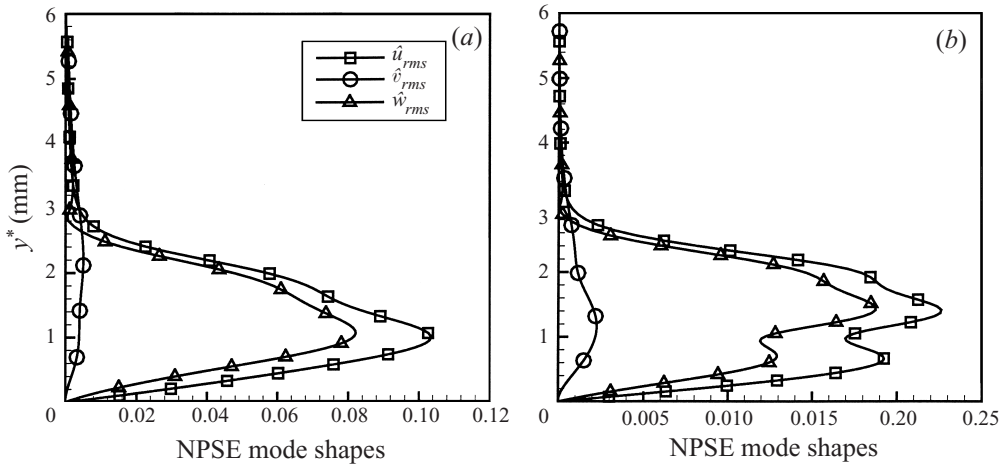


FIGURE 5. NPSE mode shapes ($\hat{u}_{rms}$, $\hat{v}_{rms}$ and $\hat{w}_{rms}$) for (*a*) mode (0, 1), and (*b*) mode (0, 2), $x^*/c = 0.35$ (symbols for reference only).

than the fundamental at the last chordwise station ($x^*/c = 0.45$) so the higher modes are considered to be unimportant for this case.

All the modes appear to grow rapidly at first, saturating at $x^*/c \approx 0.35$. This is due to the strong nonlinear interaction among the modes which occurs over a large chordwise region before the transition location reported in the experiment. It is also notable that the spanwise modes retain their amplitude ordering for the entire extent of the calculation.

At $x^*/c = 0.10$ the mean-flow distortion (0, 0) and modes (0, 2)–(0, 4) are active. For all these modes the *u*- and *w*-components are at least an order of magnitude larger than the *v*-component. In general, the number of extrema appearing in the NPSE mode shapes increases with increasing mode index indicating that a more complicated flow structure is contributed to the total disturbance by the higher modes. Figures 5(*a*) and 5(*b*) show these mode shapes for the first two modes at $x^*/c = 0.35$ in the computational coordinate system. At this location an additional 'hump' begins to appear in the (0, 1) and (0, 2) mode $\hat{u}_{rms}$ and $\hat{w}_{rms}$ profiles. This coincides with the saturation location of the maximum $\hat{u}_{rms}$ amplitudes (figure 4) and indicates a strong nonlinear interaction between the (0, 1) and (0, 2) modes. At $x^*/c = 0.40$ the additional hump has completely developed (adding two extrema) in the mode (0,1) profiles; however the additional hump in the profiles for mode (0, 2) has disappeared. The mean-flow distortion and higher modes apparently do not participate in this interaction.

Figures 6(*a*)–6(*c*) show the comparison of experimental and computational velocity contours at $x^*/c = 0.25$, $x^*/c = 0.35$, and $x^*/c = 0.45$, respectively. For these plots the ordinate is the dimensional y^*-coordinate and the abscissa is the dimensional spanwise (z^*-) coordinate (both in mm) such that the viewer is looking in the downstream direction. The contours are of the projection of the total velocity onto the (X, Y)-plane as measured in the experiment by hot-wire probes. One wavelength of the fundamental mode (12 mm) is covered in the spanwise direction and the y^*-direction is scaled so the flow structure may be examined in detail. This 'slice' of the crossflow vortex is taken in a plane which is parallel to the leading edge of the wing.

https://doi.org/10.1017/S0022112099007260 Published online by Cambridge University Press

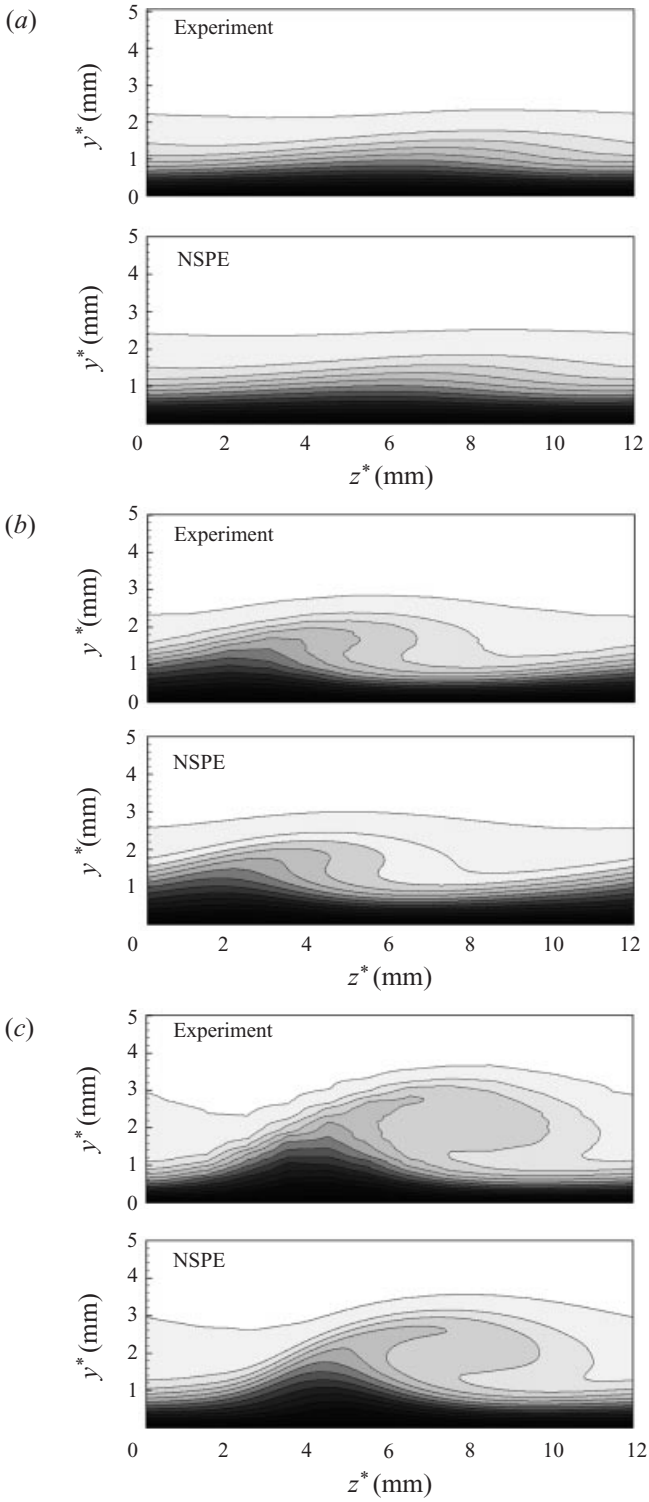


FIGURE 6. Comparison of computational and experimental total streamwise velocity contours at (*a*) $x^*/c = 0.25$, (*b*) $x^*/c = 0.35$, (*c*) $x^*/c = 0.45$.

https://doi.org/10.1017/S0022112099007260 Published online by Cambridge University Press

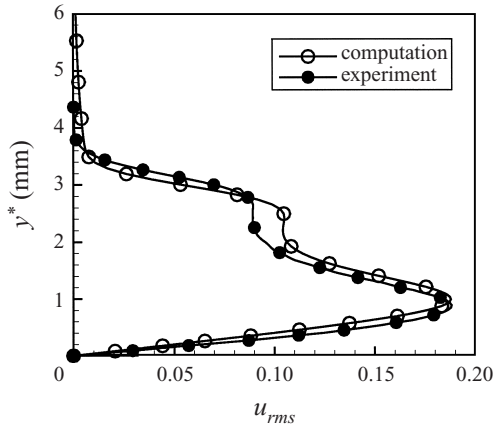


FIGURE 7. Comparison of computational and experimental disturbance u_{rms} profiles at $x^*/c = 0.45$ (symbols for reference only).

The development of these crossflow vortices occurs in two stages. For the purposes of this discussion, consider the local coordinate frame with x_{cf} aligned with the axis of the crossflow vortex, y_{cf} in the direction normal to the wall, and z_{cf} such that the coordinate system is right-handed and orthogonal. The velocity components in the x_{cf}, y_{cf}, and z_{cf} directions are denoted as u_{cf}, v_{cf}, and w_{cf}, respectively. In the first stage of crossflow development, the v_{cf} and w_{cf} components take the form of co-rotating vortices. These vortices convect low-momentum fluid away from the wall and high-momentum fluid toward the wall on the left-handside and right-handside, respectively, of the vortex axes as viewed facing downstream. That is, the 'upwelling' and 'downwelling' present in figure 6(*a*) is caused by the motion of a crossflow vortex which is rotating clockwise in this view. This first stage is *linear*.

This exchange of momentum occurs in a region very close to the wall where there are large gradients in the undisturbed velocity profile. Because of this large gradient, the small displacements caused by the v_{cf} and w_{cf} components of the disturbance eventually lead to a large u_{cf} disturbance component further downstream. This u_{cf} component soon becomes too large for nonlinear interactions to be neglected in the calculations. This is the second stage of the crossflow development. The strong nonlinear interaction between the (0, 1) and (0, 2) modes is evidenced by the roll-over occurring in the velocity contour plots, the $\hat{u}_{rms}$ maximum amplitude saturation, and the development of the additional hump in the mode (0, 1) shape functions for streamwise locations beyond $x^*/c = 0.35$ (see figures 6(*b*) and 6(*c*)).

At all streamwise locations the experimental and computational u_{rms} profiles are in excellent agreement. An example is shown in figure 7 for $x^*/c = 0.45$. These profiles are computed by taking a spanwise r.m.s average of the velocity component displayed in the contour plots above as defined by equations (2.20) and (2.21). These profiles display the disturbance growth, show the development of the additional hump, indicate the $[u_{rms}]_{max}$ amplitude saturation, and allow a more direct comparison with the experimental data than is possible with the total streamwise velocity contour plots. The additional hump in the profiles becomes noticeable at approximately $x^*/c = 0.35$, coinciding with the roll-over of the crossflow vortex and saturation of the $[u_{rms}]_{max}$ amplitude.

Figure 8 shows the experimental and computational N-factors computed using the maximum of the u_{rms} profiles along with the N-factors for LPSE and LST. From this

https://doi.org/10.1017/S0022112099007260 Published online by Cambridge University Press

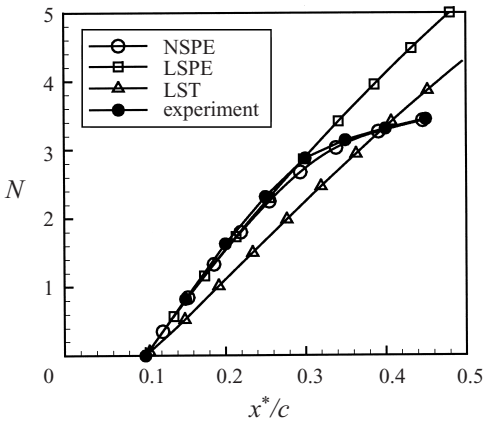


FIGURE 8. Comparison of computed and experimental N-factors, $R_C = 2.4 \times 10^6$ (symbols for reference only).

figure it is clear that both LPSE and LST fail to accurately describe the evolution of crossflow disturbances. The NPSE N-factors accurately predict the saturation of the disturbance and agree remarkably well with the experimental data. Comparing the LPSE and NPSE it is found that there is indeed a linear range of growth up to about $x^*/c = 0.25$ chord. All the computational results presented in this figure include curvature. Previous results (Arnal 1994) comparing experimental and computational N-factors using LST without curvature show a larger discrepancy than appears here.

4. Curvature, non-parallel, and nonlinear effects

There has been much debate in the literature about the effects of various curvature terms on the stability of laminar boundary layers. Some of this confusion is due to differences in notation used by different investigators. Another source of complications arises in the LST where *ad hoc* local coordinate systems are chosen to lie in either the local inviscid flow direction or in a direction such that the x-axis is aligned with the direction of wave propagation. The reader is referred to the literature for the details (Schrauf 1994, 1992; Spall & Malik 1990; Collier & Malik 1989).

The PSE formulation here utilizes a body-intrinsic coordinate system and the curvature is included in the associated metric coefficients. The marching procedure naturally aligns the disturbance wave propagation direction in the proper way as demonstrated by the agreement of experimental and computational results for the baseline case presented in the previous section. This same coordinate system is used for the LST results which are included here for comparison.

The local radius of curvature of the wing appears in the equations through the following terms:

$$k_1 = 1 + y/r_c, \quad k_2 = \frac{1}{y + r_c},$$
$$k_3 = -\frac{1}{r_c^2}\frac{\mathrm{d}r_c}{\mathrm{d}\bar{x}} \approx 0, \quad k_4 = -\frac{y}{r_c^2}\frac{\mathrm{d}r_c}{\mathrm{d}\bar{x}} \approx 0, \tag{4.1}$$

where r_c is the local dimensionless radius of curvature of the airfoil taken as positive or negative for convex or concave regions, respectively. For all the computations presented here curvature is neglected in the basic-state analysis. This is because the

https://doi.org/10.1017/S0022112099007260 Published online by Cambridge University Press

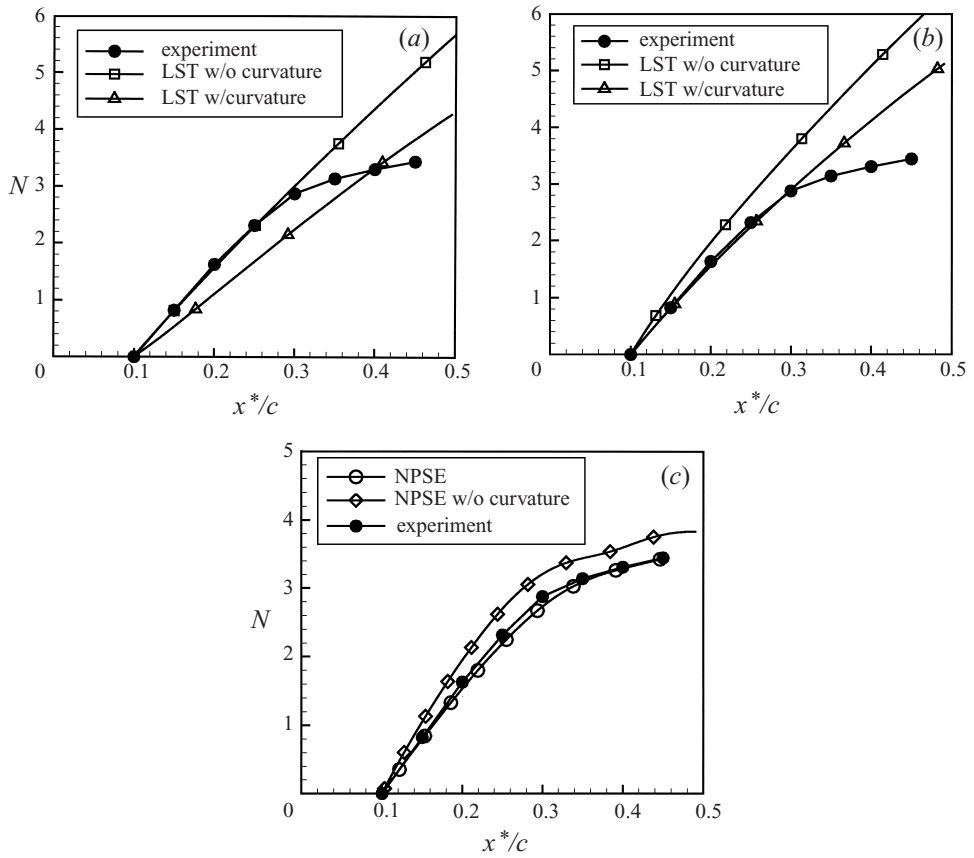


FIGURE 9. N-factors for (a) LST, (b) LSPE and (c) NSPE with and without curvature, 12 mm spanwise wavelength, $R_C = 2.4 \times 10^6$ (symbols for reference only).

basic-state curvature terms are the same order as the terms neglected according to the boundary-layer approximation so it would be inconsistent to retain them. In the limit of infinite curvature (flat plate), $r_c \to \infty$, so $k_1 = 1$ and $k_2 = 0$ are used in the stability equations for cases where curvature is neglected and equations (4.1) are used for cases where curvature is retained.

The inclusion of curvature has a very small effect on the metric coefficients for this geometry. At $x^*/c = 0.10$ the change in the metric terms k_1 and k_2 due to curvature is less than 0.5% and 0.1%, respectively. This may compel the researcher to ignore curvature effects for this geometry. However, as the following results demonstrate, even these small changes in the metric coefficients can have a significant effect on the development of crossflow vortices.

The computational results show that curvature has no significant effect on the streamwise wavenumber, but a stabilizing effect on the spatial growth rate. The stabilizing effect of curvature is demonstrated in figure 9(a) which shows the computational N-factors along with that of the experiment. Although the curvature significantly decreases the N-factor, neither LST approach properly models the crossflow disturbance evolution for this configuration since they both fail to predict the amplitude saturation.

The N-factors for LPSE with and without curvature are presented in figure 9(b) along with the experimental data. As expected, the curvature also has a stabilizing

https://doi.org/10.1017/S0022112099007260 Published online by Cambridge University Press

effect for this case. For the LPSE case the growth rates are larger than those of the LST indicating that non-parallel effects are slightly destabilizing.

As demonstrated by the N-factor comparisons for the baseline case (figure 8), proper description of the crossflow disturbance for this configuration requires the inclusion of nonlinear terms in the computations. The comparison of computational u_{rms} profiles computed with and without curvature shows development of an additional hump at an earlier streamwise location and a larger amplitude when curvature is neglected. This is not surprising since neglecting curvature leads to larger disturbance amplitudes, which in turn initiates stronger nonlinear interactions. The case without curvature also shows the roll-over of the vortices occurring at an earlier streamwise location.

Figure 9(c) shows the corresponding N-factors for the disturbance $[u_{rms}]_{max}$ amplitudes along with the experimental results. An interesting observation is that the N-factor curve for the case without curvature shows a slight 'double-saturation' whereas the calculation including curvature does not for this case. That is, because of stronger nonlinear interactions in the absence of curvature, the crossflow disturbance appears to saturate initially, then grow and saturate a second time. The fact that no double-saturation occurs in the experiment emphasizes the importance of curvature.

The results of this section demonstrate the importance of nonlinear, curvature, and non-parallel effects for this configuration. As discussed further in the following sections, curvature and non-parallel effects become increasingly important as the favourable pressure gradient is decreased.

5. Chord Reynolds number effect

Here the effect of chord Reynolds number is investigated. Again the NLF(2)-0415 airfoil with 45° sweep at −4° AOA is considered with crossflow disturbances of 12 mm fundamental spanwise wavelength. Computational results (NPSE) are presented for chord Reynolds numbers $R_C = 1.6 \times 10^6$ and $R_C = 3.2 \times 10^6$. These are compared with the experimental results of Reibert *et al.* (1996) and the baseline configuration presented earlier.

5.1. $R_C = 1.6 \times 10^6$

The chord Reynolds number and Mach number are adjusted to $R_C = 1.6 \times 10^6$ and $M = 0.044$ by decreasing the free-stream velocity from that of the baseline case ($R_C = 2.4 \times 10^6$). The NPSE calculation is performed in the same fashion as the baseline case. The disturbance is initiated by a single mode with 12 mm spanwise wavelength at $x^*/c = 0.05$ chord location. The initial condition is obtained from LST and the initial amplitude is chosen such that the disturbance $[u_{rms}]_{max}$ amplitude matches that of the experiment at $x^*/c = 0.20$. For this case the $[u_{rms}]_{max}$ amplitude is matched at $x^*/c = 0.20$ rather than $x^*/c = 0.10$ because the amplitude is too weak to be accurately measured in the experiment ahead of $x^*/c = 0.20$ for this chord Reynolds number. The results show no saturation of the crossflow disturbance for this case.

Figure 10(a) shows the comparison of computational and experimental u_{rms} profiles for several chord locations and excellent agreement is obtained. These profiles look similar at all streamwise locations and the additional hump that signified strong nonlinear interactions in the profiles of the baseline case does not appear. The corresponding N-factor is shown along with that of the experiment in figure 11(a). No evidence of saturation appears in the N-factor curves.

Figure 12(a) shows the experimental and computational u_{avg} profiles for several

https://doi.org/10.1017/S0022112099007260 Published online by Cambridge University Press

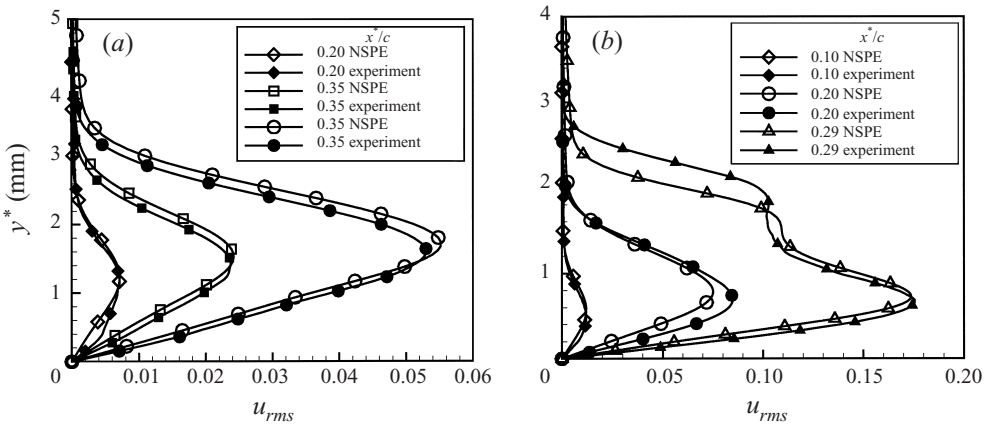


FIGURE 10. Comparison of computational and experimental disturbance u_{rms} profiles, (*a*) $R_C = 1.6 \times 10^6$, (*b*) $R_C = 3.2 \times 10^6$ (symbols for reference only).

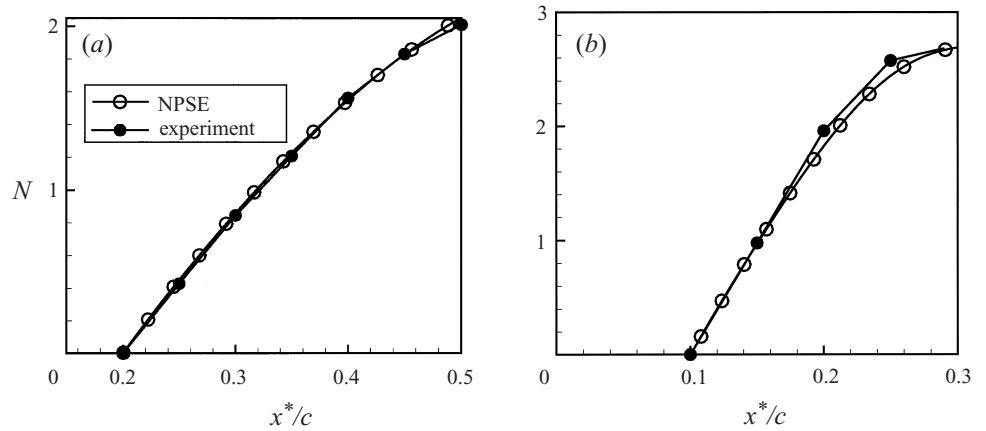


FIGURE 11. Comparison of computational and experimental N-factors, (*a*) $R_C = 1.6 \times 10^6$, (*b*) $R_C = 3.2 \times 10^6$ (symbols for reference only).

streamwise locations. The profiles are free of any measurable mean-flow distortion. This reaffirms the linear nature of the disturbance for this R_C. The total streamwise velocity contours show spanwise modulation, but there is no roll-over of the crossflow vortex.

5.2. $R_C = 3.2 \times 10^6$

The chord Reynolds number and Mach number are adjusted to $R_C = 3.2 \times 10^6$ and $M = 0.087$ by increasing the free-stream velocity accordingly. For this case the initial amplitude of the fundamental mode is chosen such that the $[u_{rms}]_{max}$ amplitude of the disturbance matches that of the experiment at $x^*/c = 0.10$. The $[\hat{u}_{rms}]_{max}$ amplitudes undergo strong saturation of all the modes at an earlier streamwise location than that observed in the $R_C = 2.4 \times 10^6$ case. The transition location observed in the experiment also occurs at an earlier streamwise location, $x^*/c = 0.32$, and the last experimental data set available for comparison is at $x^*/c = 0.29$.

The comparison of experimental and computational u_{rms} profiles is shown in figure 10(*b*) for several streamwise locations. As in the previous comparisons, the NPSE

https://doi.org/10.1017/S0022112099007260 Published online by Cambridge University Press

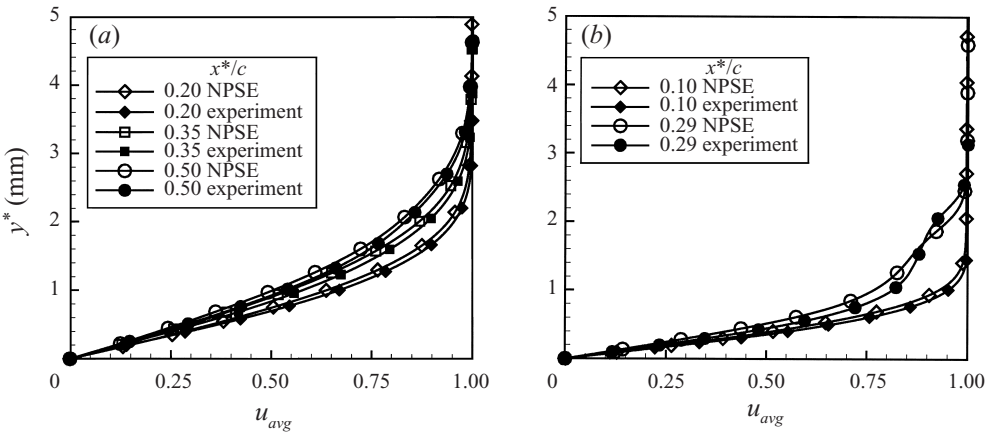


FIGURE 12. Comparison of computational and experimental u_{avg} profiles for several streamwise locations, (*a*) $R_C = 1.6 \times 10^6$, (*b*) $R_C = 3.2 \times 10^6$ (symbols for reference only).

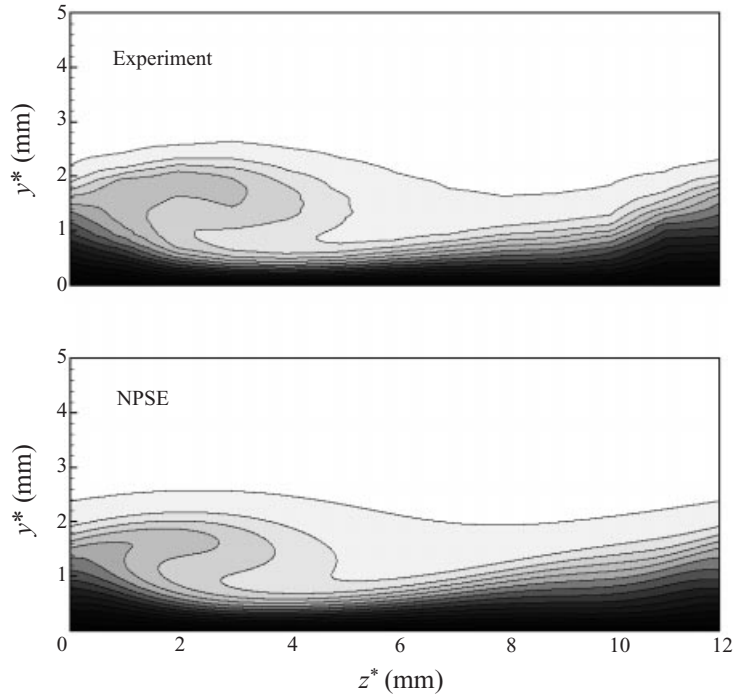


FIGURE 13. Comparison of computational and experimental total streamwise velocity contours at $x^*/c = 0.29$, $R_C = 3.2 \times 10^6$.

results show excellent agreement with the experiment. The anticipated strong nonlinear interaction causes development of the additional hump at an earlier streamwise location ($x^*/c = 0.25$) than that of the baseline case ($R_C = 2.4 \times 10^6$). The corresponding N-factors are shown in figure 11(*b*). The NPSE accurately describes the strong saturation of the crossflow disturbance for this case.

Figure 12(*b*) shows the comparison of experimental and computational u_{avg} profiles which develop the inflection due to mean-flow distortion. The comparison of

https://doi.org/10.1017/S0022112099007260 Published online by Cambridge University Press

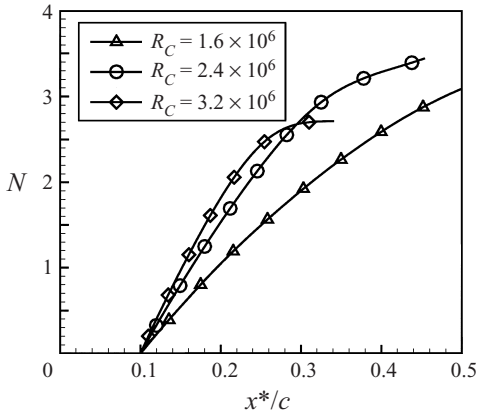


FIGURE 14. Comparison of N-factors for various Reynolds numbers (symbols for reference only).

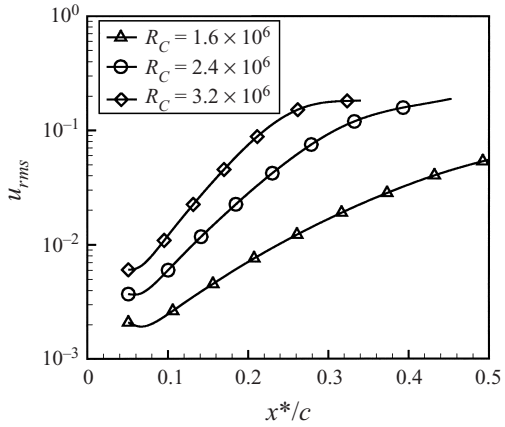


FIGURE 15. Comparison of $[u_{rms}]_{max}$ amplitudes for various Reynolds numbers (symbols for reference only).

experimental and computational total streamwise velocity contours given in figure 13 allows the best evaluation of the spanwise details of the flow field. The results here are similar to those of the baseline case except the roll-over occurs at approximately $x^*/c = 0.25$ rather than $x^*/c = 0.35$. The overall qualitative agreement is very good.

5.3. *Summary of R_C effect*

For all three cases ($R_C = 1.6 \times 10^6$, 2.4×10^6, and 3.2×10^6) the agreement between computation and experiment is excellent. The computational N-factors and $[u_{rms}]_{max}$ amplitudes for these cases are presented in figures 14 and 15, respectively. These results suggest that, for this configuration, there is a threshold chord Reynolds number above which the disturbance will saturate and below which no saturation will take place and the disturbance will evolve in a linear fashion. Clearly $R_C = 1.6 \times 10^6$ is below this threshold and the resulting disturbance field is predominantly linear. The $R_C = 2.4 \times 10^6$ case is just over the threshold showing definitely strong nonlinear interactions but weak amplitude saturation. The $R_C = 3.2 \times 10^6$ case exceeds the

https://doi.org/10.1017/S0022112099007260 Published online by Cambridge University Press

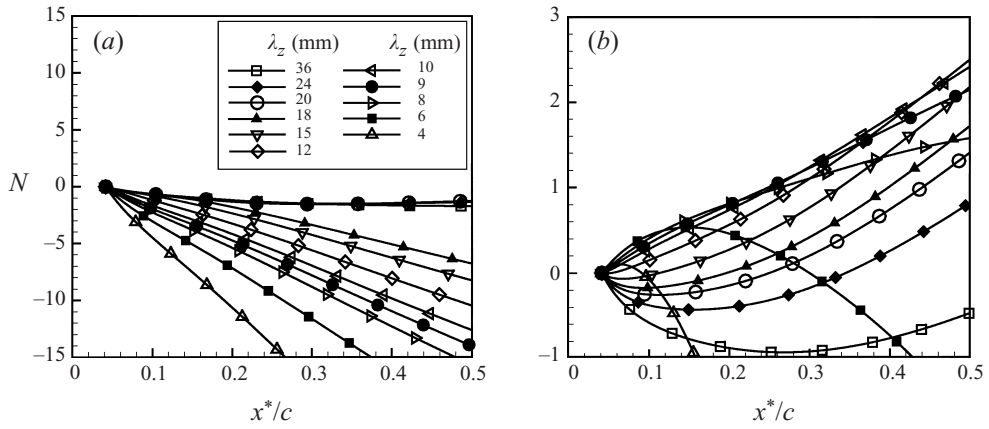


FIGURE 16. Computed LST N-factors for several spanwise wavelengths (λ_z), (a) with curvature and (b) without curvature, AOA $= -1^\circ$, $R_C = 2.4 \times 10^6$ (symbols for reference only).

threshold and exhibits strong nonlinear interactions and strong saturation with the growth of the disturbance $[u_{rms}]_{max}$ amplitude levelling off at $x^*/c \approx 0.25$.

Figure 15 suggests that there may be an 'equilibrium' disturbance $[u_{rms}]_{max}$ amplitude associated with this configuration. Both the $R_C = 2.4 \times 10^6$ and $R_C = 3.2 \times 10^6$ cases show saturation at $[u_{rms}]_{max} \approx 0.18$. This is in spite of the fact that the initial amplitudes, saturation locations, and chord Reynolds numbers are substantially different. It is also important to note that, for a given experimental roughness configuration, increasing R_C also results in an increase in the initial disturbance amplitude. If the roughness height is fixed, as it is for this investigation at $h = 6\,\mu$m, increasing R_C increases the ratio of the roughness height to the boundary-layer thickness at the location of the forcing. This results in a larger initial disturbance amplitude at the location of the forcing. The effect of initial conditions is a subject for further investigation.

6. Effect of pressure gradient

Here the effect of AOA is studied by comparing NPSE results for the baseline configuration (AOA of -4°) with those for AOA of -2° and -1°. The free-stream conditions, initial amplitude, and spanwise wavelength of the baseline configuration are used. No experimental data are available for these configurations. The objective here is to assess the effect of the pressure gradient on the crossflow disturbance.

The N-factors for AOA of -2° and several spanwise wavelengths were computed according to LST and showed a dramatic decrease in growth rates for all spanwise wavelengths compared to the AOA $= -4^\circ$ case. The 12 mm mode still has the largest N-factor at $x^*/c = 0.50$. NPSE results at this AOA show no evidence of saturation or strong nonlinear interactions, indicating that this configuration is predominantly linear. The u_{rms} profiles indicated linear disturbance behaviour since they did not display the additional hump associated with strong nonlinear interactions.

The AOA is further adjusted to -1° and the subject of curvature is revisited. Figures 16(a) and 16(b) present the LST results for -1° AOA with and without curvature terms included. The effect of curvature for this configuration is quite dramatic. The N-factor at $x^*/c = 0.45$ for the 12 mm spanwise wavelength changes from negative 10.5 to positive 2.5 when curvature is neglected. The disturbances with longer spanwise

https://doi.org/10.1017/S0022112099007260 Published online by Cambridge University Press

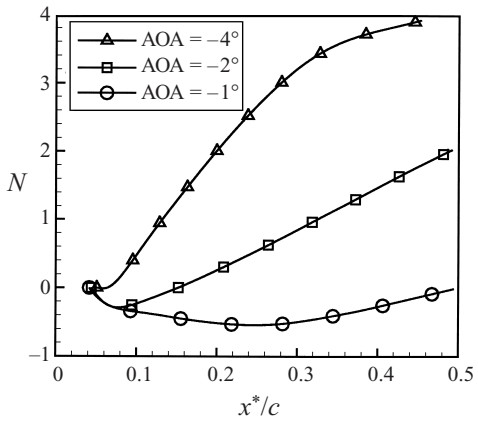


FIGURE 17. NPSE N-factors for several angles-of-attack, 12 mm fundamental spanwise wavelength (symbols for reference only).

wavelengths are not as dramatically affected. Another important consequence is the shift of the dominant spanwise wavelength predicted by LST. At $x^*/c = 0.50$, the dominant spanwise wavelength according to LST with curvature is approximately 20 mm in contrast to 12 mm for the case without curvature. The NPSE results are similar to those for $-2°$ AOA except that the crossflow disturbance is even weaker; the disturbance is not even detectable in plots of total streamwise velocity contours.

Figure 17 shows the effect of AOA on the NPSE N-factors for the three cases studied here. It is important to note that for AOA $= -2°$ and AOA $= -1°$ the NPSE results are essentially linear. The magnitude of the largest harmonic for the case of AOA $= -1°$ is three orders of magnitude smaller than the fundamental. Since the NPSE calculation for AOA $= -1°$ is essentially linear, comparing the N-factors from figures 17 and 16(a) (for 12 mm spanwise wavelength) shows that the non-parallel effects are strongly destabilizing. As mentioned previously, the effect of curvature for this case is strongly stabilizing. The disturbance is extremely sensitive to both curvature and non-parallel effects, and they must be included in the computations if accurate stability results are to be achieved. The sensitivity of the crossflow disturbance for AOA $= -1°$ prompts a closer examination of the results of Radeztsky *et al.* (1994) for this same airfoil (NLF(2)-0415) at AOA $= 0°$.

7. Comparison with Radeztsky *et al.*

The key results of the previous section should not be overlooked since they explain the large discrepancies between the experimental and computational results of Radeztsky *et al.* (1994) (see also Radeztsky 1994). Here N-factor comparisons between experiment, LPSE (without curvature), and LST (with and without curvature) show severe disagreement. The experiments were performed for the NLF(2)-0415 airfoil with 45° sweep, 0° AOA, and $R_C = 3.0 \times 10^6$. However, the stability calculations were performed for $-1°$ AOA and $R_C = 3.2 \times 10^6$ to adjust for slight differences in the computational and experimental basic states. Radeztsky *et al.* (1994) suggest that the discrepancies between the computational and experimental stability results are due to nonlinear effects. However, the experimental disturbance mode shapes have no additional humps or other features that would indicate strong nonlinear interactions.

https://doi.org/10.1017/S0022112099007260 Published online by Cambridge University Press

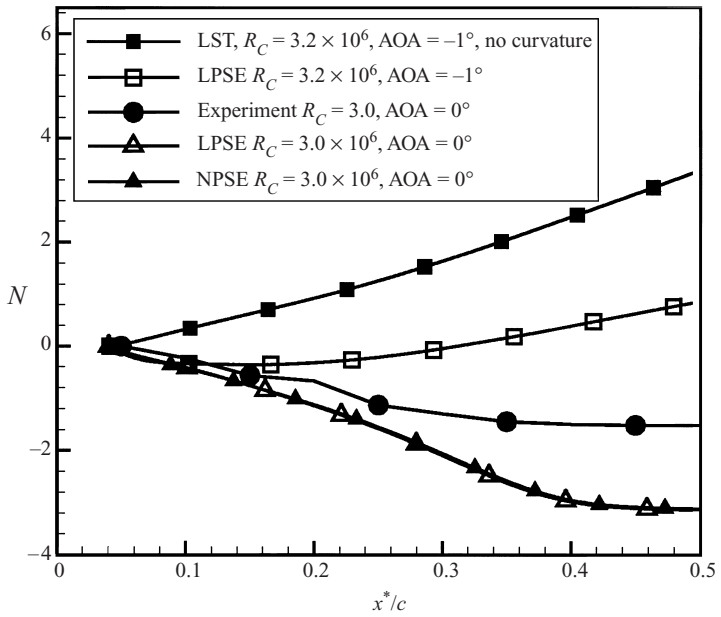


FIGURE 18. Comparison of N-factors with results of Radeztsky *et al.* (1994), AOA=0°, $R_C = 3.0 \times 10^6$, 12 mm fundamental spanwise wavelength (symbols for reference only).

In this section NPSE, LPSE, and LST results for the NLF(2)-0415 airfoil at 0° AOA and $R_C = 3.0 \times 10^6$ are presented and compared with the results of Radeztsky *et al.* (1994) in order to resolve the discrepancies. Figure 18 shows the comparison of computational N-factors with those of Radeztsky *et al* (1994) for $R_C = 3.0 \times 10^6$ and AOA $= 0°$. The LST N-factor for $R_C = 3.2 \times 10^6$ at $-1°$ AOA without curvature is included to show the wide discrepancy encountered previously. The experimental results show a decaying crossflow disturbance in sharp contrast to the growing disturbance predicted by the LST calculation.

LPSE results (with curvature) are included for two flow configurations: (i) the configuration corresponding to the actual experimental configuration with no adjustments for basic-state differences ($R_C = 3.0 \times 10^6$, AOA $= 0°$) and (ii) the configuration corresponding to the 'corrected' basic-state flow according to Radeztsky *et al.* (1994) ($R_C = 3.2 \times 10^6$, AOA $= -1°$). Figure 18 shows that the experimental N-factor curve lies between those of the former and latter cases suggesting that the basic-state corrections may have been too severe. The NPSE N-factor for $R_C = 3.0 \times 10^6$ and AOA $= 0°$ is also included in the figure and follows closely the corresponding LPSE N-factor curve confirming the linear nature of the disturbance for this configuration.

Several important conclusions are in order. First, the nonlinear interactions are not in fact the cause of the discrepancies between the previous computational and experimental results. The LPSE calculations presented here show much better agreement than was obtained by previous attempts using LST due to the inclusion of both curvature and non-parallel effects. Furthermore, NPSE and LPSE results are in agreement indicating that nonlinear interactions are unimportant for this configuration. Second, for the NLF(2)-0415 swept airfoil with AOA near 0°, the 12 mm spanwise-wavelength crossflow disturbances are incredibly sensitive to changes in AOA, R_C, and inclusion of non-parallel and curvature terms in the stability calculations. Finally, it should also

https://doi.org/10.1017/S0022112099007260 Published online by Cambridge University Press

be noted that neglecting curvature causes a significant shift in the dominant spanwise wavelength for cases near 0° AOA.

8. Conclusions

The NPSE results presented here explain the discrepancy between experimental and theoretical stability results encountered by previous investigators (Arnal 1994; Reibert *et al.* 1996). The major effect appears to be nonlinear saturation of the crossflow disturbance. The NPSE results accurately capture the saturation of the crossflow disturbance while the linear theories show no saturation for cases with a strong favourable pressure gradient (−4° AOA). This confirms the importance of nonlinearity for this case. However, an upstream region of linear growth does appear for the small-amplitude initial conditions studied here. The nonlinear interaction is strongest between the fundamental spanwise mode and its first harmonic (modes (0, 1) and (0, 2)) and leads to vortex roll-over and an additional hump in the streamwise disturbance velocity mode shapes.

Increasing the chord Reynolds number leads to earlier saturation and stronger nonlinear interactions. Results presented here suggest the existence of an 'equilibrium' state for cases with $R_C > 2.4 \times 10^6$. For lower values of R_C the disturbance behaves linearly. For $R_C = 2.4 \times 10^6$, non-parallel and curvature effects are found to be more important as the favourable pressure gradient is reduced. For cases near AOA = 0° the NLF(2)-0415 configuration is extremely sensitive to these effects.

Previous experimental and complementary computational investigations (Radeztsky *et al.* 1994) of crossflow disturbances for cases with a weak favourable pressure gradient (AOA > −1°) indicate that the crossflow disturbance is *decaying* in contrast to predictions by linear theories (LST with and without curvature and LPSE without curvature). Radeztsky *et al.* (1994) suggest that the disagreement is due to nonlinear effects. Paradoxically, the experimentally measured disturbance u_{rms} profiles indicate linear behaviour since they are lacking the development of an additional hump. The results presented here confirm that the crossflow disturbance does decay and the observed discrepancies are caused by the strong sensitivity of the crossflow disturbance to changes in curvature, non-parallel, and pressure gradient (AOA) effects. The NPSE and LPSE results indicate that the disturbance is in fact linear for this case.

The NPSE has proven to be a valuable tool for efficiently obtaining detailed disturbance velocity fields without the overhead and complications associated with direct numerical simulations. The agreement with experimental results presented here is a testament to the accuracy of the NPSE for convective instabilities. However, the NPSE relies on initial conditions from experiment or receptivity analysis. Efficient determination of initial conditions for the NPSE is an active research topic.

Through this work, a detailed quantitative comparison and validation of NPSE with a careful experiment has now been provided for three-dimensional boundary layers. Moreover, the results validate the experiments of Reibert *et al.* (1996), and Radeztsky *et al.* (1993, 1994) suggesting that their databases can be used by future researchers to verify theories and numerical schemes. The results show the inadequacy of linear theories for modelling these flows for significant crossflow amplitude and demonstrate the effects of weak curvature to be more significant than slight changes in basic state, especially near neutral-stability locations.

This work was supported by NASA Ames Research Center (NTG 50745) and the National Science Foundation Faculty Awards for Women in Science and Engineering (MSM 8696053-03). The authors also thank Dr William Saric for his physical insights,

https://doi.org/10.1017/S0022112099007260 Published online by Cambridge University Press

especially on curvature, and Dr Mark Reibert for facilitating the comparison with his experimental results.

REFERENCES

Arnal, D. 1994 Boundary layer transition: predictions based on linear theory. In *Special Course on Progress in Transition Modelling*, *AGARD Rep.* 793.

Arnal, D., Casalis, G., Reneaux, J. & Cousteix, J. 1997 Laminar-turbulent transition in subsonic boundary layers: research and applications in France. *AIAA Paper* 97-1905.

Bertolotti, F. P. 1990 Linear and nonlinear stability of boundary layers with streamwise varying properties. PhD thesis, The Ohio State University.

Bertolotti, F. P. 1996 On the birth and evolution of disturbances in three-dimensional boundary layers. In *Nonlinear Instability and Transition in Three-Dimensional Boundary Layers* (ed. P. W. Duck & P. Hall), pp. 115–132. Kluwer.

Bippes, H. 1991 Experiments on transition in three-dimensional accelerated boundary-layer flows In *Proc. R.A.S. Boundary Layer Transition and Control, Cambridge, UK*. (ed. M. Gaster). R.A.S.

Bippes H. & Müller B. 1990 Disturbance growth in an unstable three-dimensional boundary layer. In *Numerical and Physical Aspects of Aerodynamics Flows IV* (ed. T. Cebeci). Springer.

Bippes, H., Müller, B. & Wagner, M. 1991 Measurements and stability of the disturbance growth in an unstable three-dimensional boundary layer. *Phys. Fluids* A **3**, 2371–2377.

Bridges T. J. & Morris P. J. 1984 Differential eigenvalue problems in which the parameter appears nonlinearly. *J. Comput. Phys.* **55**, 437–460.

Collier, F. S. & Malik, M. R. 1989 Curvature effects on the stability of laminar three-dimensional boundary layers. In *Fluid Dynamics of Three-Dimensional Turbulent Shear Flows and Transition. AGARD CP*-438.

Deyhle, H., Höhler, G. & Bippes, H. 1993 Experimental investigation of instability wave-propagation in a 3-D boundary-layer flow. *AIAA J.* **31**, 673.

Haynes, T. S. 1996 Nonlinear stability and saturation of crossflow vortices in swept-wing boundary layers. PhD thesis, Arizona State University.

Herbert, T. 1994 Parabolized stability equations. In *Special Course on Progress in Transition Modelling. AGARD Rep.* 793.

Herbert, T. 1994 Parabolized stability equations. *Ann. Rev. Fluid Mech.* **29**, 245–283.

Kachanov, Y. S. & Tararykin, O. I. 1990 The experimental investigation of stability and receptivity on a swept wing flow. In *Laminar-Turbulent Transition* (ed. D. Arnal & R. Michel). Springer.

Mack, L. M. 1969 Boundary layer stability theory. *Tech. Rep.* 900–277 rev. A. JPL.

Malik, M. R. 1997 Boundary-layer transition prediction toolkit. *AIAA Paper* 97-1904.

Malik, M. R., Chuang, S. & Hussaini M. Y. 1982 Accurate numerical solution of compressible, linear stability equations. *J. Appl. Math. Phys.* **33**, 189.

Müller, B. & Bippes, H. 1989 Experimental study of instability modes in a three-dimensional boundary layer. In *Fluid Dynamics of Three-Dimensional Turbulent Shear Flows and Transition. AGARD CP*-438.

Pruett, D. C. & Streett, C. L. 1991 A spectral collocation method for compressible, non-similar boundary layers. In *Intl J. Numer. Meth. Fluids* **13**, 713–737.

Radeztsky, R. H. 1994 Growth and development of roughness-induced stationary crossflow vortices. PhD thesis, Arizona State University.

Radeztsky, R. H., Reibert, M. S. & Saric, W. S. 1994 Development of stationary crossflow vortices on a swept wing. *AIAA Paper* 94-2373.

Radeztsky, R. H., Reibert, M. S., Saric, W. S. & Takagi, S. 1993 Effect of micron-sized roughness on transition in swept-wing flows. *AIAA Paper* 93-0076.

Reed, H. L., Saric, W. S. & Arnal, D. 1996 Linear stability theory applied to boundary layers. *Ann. Rev. Fluid Mech.* **28**, 389–428.

Reibert, M. S. 1996 Nonlinear stability, saturation, and transition in crossflow-dominated boundary layers. PhD thesis, Arizona State University.

Reibert, M. S., Saric W. S., Carrillo, R. B. & Chapman, K. L. 1996 Experiments in nonlinear saturation of stationary crossflow vortices in a swept-wing boundary layer. *AIAA Paper* 96-0184.

https://doi.org/10.1017/S0022112099007260 Published online by Cambridge University Press

Schrauf, G. 1992 Curvature effects for three-dimensional compressible boundary-layer stability. *Z. Flugwiss. Weltraumforsch.* **16**, 119–127.

Schrauf, G. 1992 On wave-front curvature in linear stability theory. *La Recherche Aérospatiale* **2**, 153–158.

Spall, R. & Malik, M. 1990 Effect of transverse curvature on the stability of compressible boundary layers. *AIAA Paper* 90-1446.

Stevens, W. A., Goradia, S. H. & Braden, J. A. 1971 A mathematical model for two-dimensional multi-component airfoils in viscous flow. *NASA CR*-1843.

https://doi.org/10.1017/S0022112099007260 Published online by Cambridge University Press